Editors' Suggestion

Excited-state geometry relaxation of point defects in monolayer hexagonal boron nitride

Alexander Kirchhoff,* Thorsten Deilmann, and Michael Rohlfing
Institute of Solid State Theory, University of Münster, Wilhelm-Klemm-Straße 10, 48149 Münster, Germany

(Received 22 September 2023; revised 19 December 2023; accepted 25 January 2024; published 16 February 2024)

Point defects in hexagonal boron nitride (hBN) are often discussed as single-photon emitters for quantum technologies. Understanding the dependence of electronic and optical properties on the geometry might help to identify the atomic structure of the defects and is also crucial in order to make these emitters applicable. Here, we study three defects in a monolayer of hBN, namely, C_BV_N, C_BC_N, and C_BO_N, from an *ab initio* approach. We use (constrained) density functional theory to obtain optimal geometries of the electronic ground state and the first excited state and then refine quasiparticle energies and optical excitation energies using a *GW* and Bethe-Salpeter equation (BSE) based approach. All three defect systems host transitions between deep-lying defect states. We find the lowest defect exciton of C_BC_N at ∼4 eV and of the other two defects at ∼2 eV with significant Stokes shifts of 0.15 and 0.79 eV, respectively. Finally, we investigate the effects of the Tamm-Dancoff approximation and show that it can have a significant influence on hBN defect excitons calculated from BSE.

DOI: 10.1103/PhysRevB.109.085127

I. INTRODUCTION

Hexagonal boron nitride (hBN) is a van der Waals material with an optical gap of about 6 eV [1]. The attention to point defects in this material has increased in the past decade due to their potential use as room-temperature stable two-dimensional (2D) single-photon emitters for quantum computing [2–4]. Recently, progress has been made in the fabrication of hBN quantum emitters with reproducible and controllable properties and their integration into quantum circuits [5–11]. The tunability of properties of quantum emitters, e.g., by electric fields [12] or by strain [13–15], is a desirable feature for quantum technological applications. Conversely, this tunability contributes to the understanding of the atomic structure of the defect, which still poses an unsolved problem due to the variety of properties of hBN emitters. The observation of Stark shift with an electric field perpendicular to the layers of hBN means that some defects may break the planar symmetry of the 2D material [16]. Phonon side bands [17] or the influence of the emitter's distance to flake boundaries [18] are specific to the atomic structure.

The equilibrium atom positions depend on the electronic configuration and therefore differ between ground and excited states [19], so that optical measurements do not probe the energy difference between ground and excited states only at fixed geometry. Figure 1 shows the vertical transition energies on the absorption (T_v) and emission ($T_{v'}$) sides, as well as the zero-phonon line (ZPL), which is also referred to as adiabatic transition energy T_e. While photoluminescence (PL) [20] mainly probes the emission side [21], optical absorption [22] and photoluminescence excitation spectroscopy (PLE) [23,24] probe the absorption side.

Theoretical *ab initio* calculations of ground- and excited-state curves are mainly based on density functional theory (DFT) [16,25–29] or more accurate wave function methods [30,31]. The latter are usually employed for molecules or model compounds. Many-body perturbation theory (MBPT) has been widely used to study hBN defects [32–37], but so far their dependence on geometry has rarely been studied. In this work, we combine the two fields: We start with DFT to obtain the optimal geometries for the ground and excited states and then use MBPT (*GW*-Bethe-Salpeter equation) to improve the total energies for the excited state for selected geometries [38]. Motivated by the finding that carbon appears to be a prominent impurity of hBN [9,39], we focus on systems of the type C_BX_N, with X being a carbon or oxygen substitution (C or O) or a vacancy (V) on the nitrogen site, while a carbon substitution resides on the adjacent boron site. All defects are studied with the neutral charge configuration. Both C_BV_N [16,27,28,30,40] and C_BC_N [26,41] have been proposed as quantum emitters and thus have been studied in the literature. Besides carbon, oxygen has been proposed to be part of the hBN impurities as well [42,43], and oxygen-based defects have been analyzed in theory [28,33,44]. But to the best of our knowledge, no *ab initio* study has been carried out on C_BO_N yet. Our motivation to study C_BO_N is supported by the fact

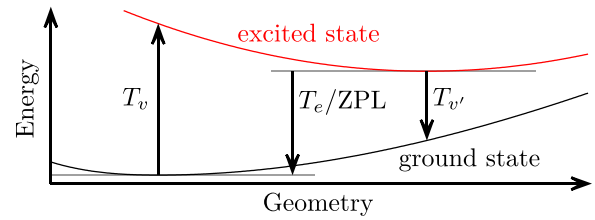

FIG. 1. Scheme of absorption and emission energies.

*alexander.kirchhoff@uni-muenster.de

that urea is used to synthesize hBN flakes [45], and the N_2CO fragment in the urea molecule is the same as in the defect.

Our work is structured as follows: After introducing our methods in Sec. II, we apply them to an isolated carbon monoxide (CO) molecule in the gas phase in Sec. III. In contrast to the defect systems, CO has a one-dimensional configuration space, which is spanned by the bond length. In Sec. IV, we analyze C_BC_N, C_BO_N, and C_BV_N: Starting with DFT, we obtain geometries and a first approximation of the single-particle energies (band structure). We improve the latter within the LDA + GdW approach, which is an efficient approximation of the GW method. Optical properties like excitons and absorption spectra are then obtained by solving the Bethe-Salpeter equation (BSE). The BSE excitation energies are added to the DFT ground-state total energy to obtain the MBPT excited-state total energy. In Sec. V, we discuss the validity of the Tamm-Dancoff approximation (TDA) within the BSE for defects in hBN.

II. METHODS

The aim of this work is to calculate the total energy of the ground and first excited states. DFT is known for reliable structure optimizations and ground-state energies, which is why we rely on the optimized geometries of both the ground and excited states calculated in DFT. However, it does not incorporate many-body effects precisely, which results in an underestimation of the band gap [46]. Therefore, we refine the total energies for the excited states with methods from MBPT. To be more precise, we use a GW-based ansatz to obtain single-particle excitation energies and use these results to set up and solve the BSE, which provides improved energies of the excited state [38]. In the following, we explain the theoretical details of our approaches.

A. Density functional theory

We perform DFT calculations within the local density approximation (LDA) [47]. For spin-polarized configurations like excited triplet states, we use the local spin-density approximation (LSDA) [48]. We employ norm-conserving pseudopotentials [49–52] and a basis set of atom-centered Gaussian orbitals [53].

In DFT, single-particle orbitals $\psi_{\mathbf{n},\sigma}(\mathbf{r})$ and energies $\epsilon^{\mathrm{DFT}}_{\mathbf{n},\sigma}$ are obtained by solving the Kohn-Sham equations [54]. The index $\mathbf{n} = (n, \mathbf{k}_n)$ combines the band number and k point, and $\sigma = \uparrow, \downarrow$ denotes the spin, which is a good quantum number in the absence of spin-orbit coupling. Within LSDA, the total energy is calculated via [55]

$$E^{\mathrm{DFT}}_{\mathrm{tot}} = \sum_{\mathbf{n},\sigma} f_{\mathbf{n},\sigma} \langle \psi_{\mathbf{n},\sigma} | -\frac{1}{2}\nabla^2 | \psi_{\mathbf{n},\sigma} \rangle + U[\rho_\uparrow, \rho_\downarrow]. \tag{1}$$

The functional U depends on the electron densities in both spin channels,

$$\rho_\sigma(\mathbf{r}) = \sum_{\mathbf{n}} f_{\mathbf{n},\sigma} |\psi_{\mathbf{n},\sigma}(\mathbf{r})|^2, \tag{2}$$

and $f_{\mathbf{n},\sigma}$ are occupation numbers. In spin-unpolarized systems (i.e., closed-shell configurations), the occupation numbers and orbitals no longer depend on the spin, and the sum over σ in Eqs. (1) and (2) yields a factor of 2. The functional U then solely depends on the total electron density $\rho = \rho_\uparrow + \rho_\downarrow$.

If the number of electrons per unit cell is N, then the ground state of a semiconductor with a sufficiently large gap has $f_{\mathbf{n},\sigma} = 1$ for the N energetically lowest bands and $f_{\mathbf{n},\sigma} = 0$ otherwise. For excited states, the occupation numbers change, which we refer to as constrained DFT (cDFT) [56,57]. We note that alternative nomenclature may be used in the literature [29]. We restrict ourselves to transitions between intragap defect states such that bands are either completely occupied or completely empty. We mainly use cDFT with a spin-unpolarized variant; i.e., if an orbital is occupied by one electron, it is distributed on both spin channels equally, which approximates a singlet state [58,59]. If $\mathbf{v}$ denotes the valence state which is depopulated by one electron and $\mathbf{c}$ is the conduction state which is occupied by one electron, the occupation numbers are $f_{\mathbf{v},\sigma} = f_{\mathbf{c},\sigma} = 0.5$. Excited triplet states are described within LSDA-cDFT, occupying both levels in the same spin channel, e.g., the spin-up channel: $f_{\mathbf{v},\uparrow} = f_{\mathbf{c},\uparrow} = 1$ and $f_{\mathbf{v},\downarrow} = f_{\mathbf{c},\downarrow} = 0$. In both DFT and cDFT, we use the same structure optimization algorithm [60]. By minimizing the total energy of the ground or excited state, we obtain the respective optimal geometry, denoted by $\mathbf{R}^{(\mathrm{g})}_\mu$ or $\mathbf{R}^{(\mathrm{e})}_\mu$, where μ denotes the atom in the unit cell. To discuss geometrical dependence, we linearly change the geometry via a dimensionless parameter α,

$$\mathbf{R}^{(\alpha)}_\mu = \mathbf{R}^{(\mathrm{g})}_\mu + \alpha\left(\mathbf{R}^{(\mathrm{e})}_\mu - \mathbf{R}^{(\mathrm{g})}_\mu\right), \tag{3}$$

and plot total energies or other electronic quantities as a function of the configuration coordinate [61]:

$$q^{(\alpha)} = \mathrm{sgn}(\alpha)\sqrt{\sum_\mu M_\mu \left|\mathbf{R}^{(\alpha)}_\mu - \mathbf{R}^{(\mathrm{g})}_\mu\right|^2}, \tag{4}$$

where M_μ is the atomic mass. Of special interest to the discussion of the difference between ground and excited states is the total configuration coordinate ΔQ, which was, for example, defined in [19]:

$$\Delta Q = q^{(1)} = \sqrt{\sum_\mu M_\mu \left|\mathbf{R}^{(\mathrm{e})}_\mu - \mathbf{R}^{(\mathrm{g})}_\mu\right|^2}. \tag{5}$$

B. Many-body perturbation theory

The single-particle energies $\epsilon^{\mathrm{DFT}}_{\mathbf{n},\sigma}$ are improved within the "one-shot" GW approximation (in the literature often called G_0W_0) [62,63]. This was already applied to pristine hBN in previous work [64]. In short, the exchange correlation potential from DFT V_{xc} is replaced by the self-energy Σ:

$$\epsilon^{GW}_{\mathbf{m}} = \epsilon^{\mathrm{DFT}}_{\mathbf{m}} + \langle \psi_{\mathbf{m}} | \Sigma\left(\epsilon^{GW}_{\mathbf{m}}\right) - V_{\mathrm{xc}} | \psi_{\mathbf{m}} \rangle, \tag{6}$$

where the spin index has been subsumed in $\mathbf{m} = (\mathbf{n}, \sigma)$. Equation (6) employs the approximation that $\Sigma - V_{\mathrm{xc}}$ is diagonal in the LDA wave functions $|\psi_{\mathbf{m}}\rangle$. Taking nondiagonal elements into account for the calculation of $\epsilon^{GW}_{\mathbf{m}}$, we find no significant changes for the systems studied in this work. We refer to the Supplemental Material for further details [65]. The self-energy is approximated by the single-particle Green's function G times the screened Coulomb potential W: $\Sigma = iGW$. The screened Coulomb potential is calculated by convoluting the

bare Coulomb interaction with the inverse dielectric function. The latter is obtained from random-phase approximation [66,67]. Renormalization due to the energy dependence of Σ has been taken into account [65]. For the CO molecule, all quantities are evaluated in real space via a Gaussian basis set.

For the defect systems, we employ the LDA + GdW approach [68] as a fast approximation of GW because they are more demanding due to the need for large supercells. Instead of calculating Σ, the difference $\Sigma - V_{\mathrm{xc}}$ is approximated by $iG(W - W_{\mathrm{metal}})$, motivated by the observation that iGW_{metal} reproduces the exchange-correlation functional in LDA: $iGW_{\mathrm{metal}} \approx V_{\mathrm{xc}}^{(\mathrm{LDA})}$ [69–71]. Both W and W_{metal} are set up in a plane wave basis set from atom-resolved dielectric model functions [72,73], while the data to set up these model functions is calculated via a plasmon pole model [74,75]. In GdW, significantly fewer plane waves are needed compared to GW, which is one of the reasons why GdW is numerically less demanding. The GdW method was successfully used as a good approximation of GW for various systems [68,76,77], among them hBN [64].

Within GW, we obtain the single-particle excitation energies, which are the energies needed to remove or add an electron including the response of the system. The excited state calculated in cDFT is a two-particle excitation because, in a simple picture, an electron is removed from one orbital and added to another. In MBPT, two-particle excitations are calculated by solving the BSE [78,79]. In practice, a BSE Hamiltonian is set up in the basis of resonant transitions (or excitations, $\mathbf{v} \to \mathbf{c}$) and antiresonant transitions (or deexcitations, $\mathbf{c} \to \mathbf{v}$) from GW results [80] for the CO molecule and from GdW results for the defect systems:

$$H^{\mathrm{BSE}}_{\mathbf{vc},\mathbf{v'c'}} = \underbrace{\left(\epsilon^{GW}_{\mathbf{c}} - \epsilon^{GW}_{\mathbf{v}}\right)\delta_{\mathbf{vv'}}\delta_{\mathbf{cc'}}}_{=D_{\mathbf{vc},\mathbf{v'c'}}} + K_{\mathbf{vc},\mathbf{v'c'}}. \tag{7}$$

The indexes $\mathbf{v}$ and $\mathbf{v}'$ run over valence states, and $\mathbf{c}$ and $\mathbf{c}'$ run over conduction states. Again, each index combines the band number, k point, and spin, e.g., $\mathbf{v} = (v, \mathbf{k}_v, \sigma_v)$. The quantity K is the electron-hole interaction kernel. We restrict ourselves to excitations with zero total momentum, i.e., $\mathbf{k}_c = \mathbf{k}_v$. Diagonalizing the BSE Hamiltonian then leads to the following eigenvalue problem [81]:

$$\begin{pmatrix} D + K^{AA} & K^{AB} \\ -(K^{AB})^* & -D - (K^{AA})^* \end{pmatrix} \begin{pmatrix} A^S \\ B^S \end{pmatrix} = \Omega_S \begin{pmatrix} A^S \\ B^S \end{pmatrix}. \tag{8}$$

The coefficients A^S and B^S are for the resonant and antiresonant parts of the transitions, respectively. The eigenvalues Ω_S are the (de)excitation energies. The excited-state total energy is then obtained by adding the exciton energy to the ground-state total energy in DFT:

$$E_{\mathrm{tot,exc.}} = E^{\mathrm{DFT}}_{\mathrm{tot,ground}} + \Omega_S, \tag{9}$$

which is more precise than the energy from cDFT in Eq. (1). In Secs. III and IV, we will refer to this procedure as DFT + BSE.

The resonant-resonant (K^{AA}) and resonant-antiresonant (K^{AB}) parts of the electron-hole interaction kernel can both be split up into a direct part and an exchange part, e.g., $K^{AA} = K^{AA}_{\mathrm{d}} + K^{AA}_{\mathrm{x}}$. While the exchange part contains the bare Coulomb interaction, the direct part contains the screened Coulomb potential W in a static screening approximation. For spin-unpolarized systems, Eq. (8) decomposes into the singlet ($K_{\mathrm{d}} + 2K_{\mathrm{x}}$) and triplet ($K_{\mathrm{d}}$) subspaces [82].

The resonant-antiresonant terms are often negligible: $K^{AB} \ll D + K^{AA}$. This leads to the TDA [83] of setting $K^{AB} = 0$, and Eq. (8) reduces to one quarter of the size: $(D + K^{AA})A^S = \Omega_S A^S$. All results for CO presented in Sec. III are calculated beyond the TDA; i.e., the full BSE Hamiltonian in Eq. (8) has been diagonalized. In contrast to this, the results for the defect systems in hBN in Sec. IV are obtained within the TDA, whose validity is discussed in Sec. V.

To calculate optical spectra, we need, apart from the exciton energies Ω_S, the oscillator strengths. They are calculated via the scalar product of the momentum operator matrix elements $\langle\psi_{\mathbf{v}}|\hat{\mathbf{p}}|\psi_{\mathbf{c}}\rangle$ and the electric field vector $\mathbf{E}$. We restrict ourselves to perpendicular incoming light; i.e., $\mathbf{E}$ lies in the plane of the hBN layer. For DFT, GW, and BSE we used code we developed ourselves [53,60,66,68,72,76,81,84]. For further information about the theoretical methods used in this work and numerical details, see the Supplemental Material [65].

III. CARBON MONOXIDE

Within the Born-Oppenheimer approximation, the bond distance of diatomic molecules is the only structural coordinate on which the electronic states depend. This makes them model candidates to examine the excited states' dependence on geometry. We choose carbon monoxide (CO) as it is known to exhibit stable, nondissociating excited states [85]. Figure 2(a) shows the highest occupied and lowest unoccupied energy levels in the ground-state geometry of CO, calculated from GW. The highest occupied molecular orbital (HOMO) has σ symmetry and lies 13.3 eV underneath the vacuum level, which is slightly smaller than the experimental value for the ionization energy of CO of 14.1 eV [86]. The second-highest occupied level of π symmetry is 16.0 eV below the vacuum level. The lowest unoccupied molecular orbital (LUMO) has π^* symmetry and lies above the vacuum level. Transitions between σ and π^* lead to excited Π states; transitions between π (HOMO − 1) and π^* lead to excited Σ and Δ states. These characters are needed to distinguish the various lowest bound excited states which are calculated from the BSE and are shown in Fig. 2(c) as a function of the C-O distance. $^1\Sigma^+$ refers to the ground state which is obtained from DFT.

In Table I, we compare the equilibrium bond distances, transition energies, and oscillation frequencies of the lowest bound electronic states [65] with experimental data and theoretical studies from the literature. The equilibrium distances in Table I are in very good agreement with the literature. Taking the $^1\Pi$ state as an example, the calculated equilibrium distance is less than 2% larger than the experimental value. We note that our result is in excellent agreement with the value of 1.26 Å reported by Ismail-Beigi and Louie [87], who also applied the GW + BSE method. Looking at the transition energies T_e, our results are less than 10% lower than values in the experimental data. For the lowest singlet excited state $^1\Pi$, the deviation is only about 2%.

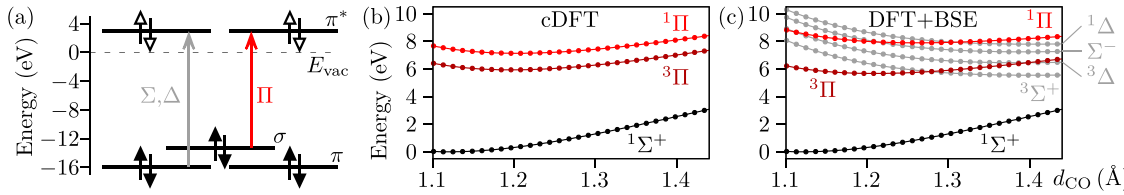

FIG. 2. Carbon monoxide. (a) Single-particle energy levels relevant for the lowest excitons, relative to the vacuum level E_{vac}. Transitions between σ (HOMO) and π^* (LUMO) lead to excited Π states; transitions between π (HOMO − 1) and π^* lead to excited Σ and Δ states. In (b) and (c), the total energies of the ground state $^1\Sigma^+$ and the lowest bound excited states of carbon monoxide are shown as a function of the C-O bond distance d_{CO}, calculated from (b) cDFT and (c) BSE. Within BSE, we additionally calculated the excited Σ and Δ states. The Σ^- state has no label for spin multiplicity because the singlet and triplet states have the same energy.

IV. DEFECTS IN hBN

In previous work [64], we presented results for a monolayer of intrinsic hBN. We optimized the lattice constant of hBN to 2.479 Å (experiment: 2.506 Å [92]). For all calculations of this work, we use the lattice constant optimized in DFT in order to prevent the structure optimization of the defect cells from being affected. The minimal gap is 4.61 eV in LDA and 6.96 eV (from K to Γ) in GdW, the latter being close to the result in G_0W_0 of 7.27 eV and in better agreement with experimental estimates of the gap [93–95]. The lowest exciton was found at 5.61 eV within GdW + BSE, in good agreement with other values reported in the literature. Table II summarizes our main results for three defects in hBN monolayers, which are analyzed in detail in the following sections. The relaxed atom positions for all systems in different electronic configurations are provided in the Supplemental Material [65].

TABLE I. Transition energies T_v and T_e (defined in Fig. 1), equilibrium bond distances $d_{CO,e}$, and the oscillation frequency in harmonic approximation ω_e of the lowest bound states of CO. Results without a reference are from this work compared to other works, including CI (configuration interaction) and CCSD (coupled-cluster singles and doubles).

State	T_v (eV)	T_e (eV)	$d_{CO,e}$ (Å)	ω_e (cm^{-1})	Method	Ref.
$^1\Sigma^+$	0	0	1.120	2171	DFT	
			1.13	2050	DFT	[87]
			1.134	2000	CI	[88]
			1.128	2170	experiment	[89]
$^3\Pi$	5.935	6.219	1.197	1802	cDFT	
	6.018	5.673	1.209	1666	BSE	
		6.203	1.192	1870	CI	[88]
		6.036	1.206	1743	experiment	[89]
$^3\Sigma^+$	7.622	5.544	1.403	980	BSE	
		6.886	1.345	1240	CI	[88]
		6.921	1.352	1229	experiment	[89]
$^3\Delta$	8.481	6.451	1.388	1073	BSE	
		7.508	1.373	1150	CI	[88]
		7.578	1.370	1172	experiment	[89]
$^1\Pi$	7.134	7.463	1.204	1760	cDFT	
	8.569	7.893	1.261	1354	BSE	
		7.02	1.21	1720	cDFT	[87]
		8.32	1.26	1290	BSE	[87]
	8.665	7.909	1.224	1593	CCSD	[90]
		8.742	1.243	1800	CI	[88]
	8.15		1.233		CI	[91]
		8.068	1.235	1518	experiment	[89]
$^1\Sigma^-$	9.298	7.241	1.392	1062	BSE	
		7.960	1.411	1050	CI	[88]
	9.71		1.419		CI	[91]
		8.069	1.391	1092	experiment	[89]
$^3\Sigma^-$	9.298	7.241	1.392	1062	BSE	
		7.775	1.390	1100	CI	[88]
		7.964	1.384	1118	experiment	[89]
$^1\Delta$	9.858	7.796	1.401	1010	BSE	
		7.962	1.412	1030	CI	[88]
	9.74		1.420		CI	[91]
		8.174	1.399	1094	experiment	[89]

A. C_BC_N

Two adjacent carbon substitutions form the C_BC_N defect (also referred to as the carbon dimer), which is depicted in Fig. 3(a). The optimal geometry of the ground state is planar. The carbon atom on the boron site gives rise to a donor level 0.37 eV underneath the intrinsic conduction band edge in GdW, while the carbon atom on the nitrogen site leads to an acceptor level 0.82 eV above the valence band edge, as can be seen in Fig. 3(b). In LDA, the respective values are 0.35 and 0.68 eV, so the gap opens from 3.58 to 5.77 eV after the GdW method is applied (intrinsic gap in LDA: 4.61 eV). We note that the wave functions plotted in Fig. 3(b) show strong similarities to the defect states observed in single-carbon substitutions C_B and C_N [64]. The point group of the system is C_{2v}. Both defect states have b_1 symmetry. The transition A between the defect states leads to the lowest exciton of the system at 4.27 eV [Fig. 3(c)], which is below the lowest

TABLE II. Overview of the properties of the three defects investigated in this work. The transition energies T_v, $T_{v'}$, and T_e (see Fig. 1) and the Stokes shift (defined as $T_v - T_{v'}$) are given in eV, while ΔQ [Eq. (5)] is given in amu$^{\frac{1}{2}}$ Å.

		T_v	$T_{v'}$	T_e	Stokes shift	ΔQ
C_BC_N	cDFT	3.74	3.55	3.65	0.19	0.21
	DFT + BSE	4.27	4.12	4.21	0.15	
C_BO_N	cDFT	2.28	1.44	1.83	0.84	1.36
	DFT + BSE	1.91	1.12	1.51	0.79	
C_BV_N	cDFT	2.08	0.28	1.23	1.80	3.46
	DFT + BSE	1.79				

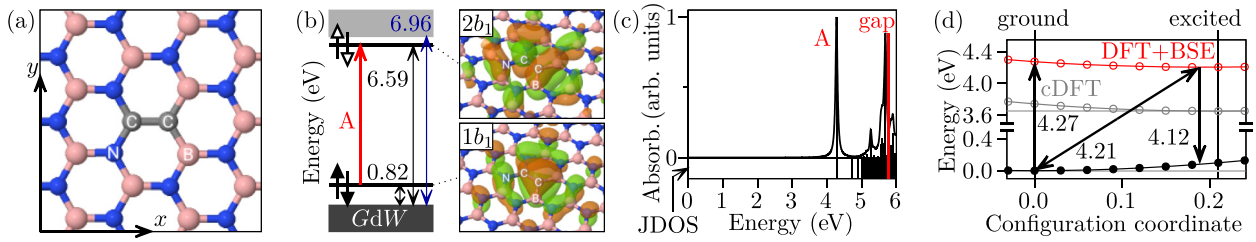

FIG. 3. C_BC_N. (a) Top view of the ground-state geometry. The system is planar. (b) Fully spin-degenerate single-particle energy levels in GdW, showing one occupied defect state and one empty intragap defect state, labeled $1b_1$ and $2b_1$. The panels on the right show these defect states in real space. The transition between them is labeled "A." The resulting defect exciton can be found in the (c) absorption spectrum at 4.27 eV, which is also the lowest exciton of the system. To visualize dark states, we show the joint density of states (JDOS) underneath the absorption spectrum. The peak at 5.6 eV resembles the lowest exciton of intrinsic hBN (see text). (d) Total energies of the ground state (solid circles) and the excited state (open circles) as a function of the configuration coordinate, defined in Eq. (4), in units of amu$^{\frac{1}{2}}$ Å. For the excited state, results from cDFT and DFT + BSE are shown. The data points of the latter were fitted with polynomials to estimate the minimum of the curve.

exciton of intrinsic hBN but outside the visible spectrum in the UV range. This agrees very well with the literature, where C_BC_N has been proposed as a candidate for UV emitters observed in experiment [26,96,97]. As Table III shows, our values for the energy levels and the transition energies are in good agreement with the literature, taking into account that gaps obtained within the Perdew-Burke-Ernzerhof (PBE) and Heyd-Scuseria-Ernzerhof (HSE) functionals are usually larger than those from LDA and slightly smaller than those from GW-based methods.

Between 5 and 6 eV in the absorption spectrum in Fig. 3(c) there are several bright peaks. The one with the strongest oscillator strength mainly stems from transitions between the highest intrinsic valence and lowest intrinsic conduction bands and can be identified as the exciton of intrinsic hBN. We note, however, that due to the finite size of the supercell the energy slightly differs (less than 0.1 eV) from the intrinsic exciton which was calculated for the pristine cell without defect.

Next, we focus on the excited state where one electron occupies $2b_1$ and one electron remains in $1b_1$. To simulate this state in DFT, we use cDFT with the spin-unpolarized variant, which approximates the singlet configuration. As for the ground state, the optimal geometry of the excited state is planar and maintains the C_{2v} symmetry. When changing the geometry from the ground state to that of the excited state, the gap in the electronic ground state decreases from 5.77 eV (3.58 eV) in GdW [cDFT(LDA)] to 5.51 eV (3.37 eV). The total energies of the ground state and the excited state change little during the geometry relaxation, as Fig. 3(d) shows. The vertical and adiabatic transition energies are in reasonable agreement with other studies (Table III). Most importantly, the minima of both curves lie close together, which justifies our approach of seeking the optimal excited state's geometry with the help of cDFT.

In previous works, the transition energies T_e and $T_{v'}$ were also obtained by adding reorganization energies calculated in cDFT or time-dependent DFT to the value of T_v obtained in BSE [41,99]. This approach slightly differs from our method, as we also perform BSE calculations for geometries other than the ground-state geometry. The reorganization energies are the energy differences of a fixed electronic state at different geometries, i.e., $T_e - T_{v'}$ for the ground state and $T_v - T_e$ for the excited state. Hence, the sum of these reorganization energies is the Stokes shift $T_v - T_{v'}$. As can be seen in Table II, the values of the Stokes shift calculated in cDFT are in reasonable agreement with the Stokes shifts obtained from DFT + BSE.

TABLE III. C_BC_N. Comparison of energy levels $1b_1$ and $2b_1$ [see Fig. 3(b)], the gap of intrinsic hBN ("Gap"), vertical (T_v and $T_{v'}$) and adiabatic (T_e) transition energies, and the total configuration coordinate. All energies are in eV; ΔQ is in amu$^{\frac{1}{2}}$ Å. Results without reference are from this work. DFT + GdW/BSE is equivalent to DFT + BSE. The last row contains an experimentally observed ZPL of defect-related emission in hBN, which lies close to the calculated adiabatic transition energies of C_BC_N.

Ref.	$1b_1$	$2b_1$	Gap	T_v	$T_{v'}$	T_e	ΔQ
cDFT(LDA)	0.68	4.26	4.61	3.74	3.55	3.65	0.21
DFT + GdW/BSE	0.82	6.59	6.96	4.27	4.12	4.21	0.19
[41], cDFT(PBE)	0.5	4.0	4.71				
[41], G_0W_0/BSE	1.7	8.0	7.29	4.44		4.32	
[98], cDFT(PBE)				3.44	3.20	3.34	0.28
[26], cDFT(HSE)	0.77	6.00	6.42	4.53	4.07	4.31	
[99], evGW/BSE			7.87	4.51	4.20	4.36	
[97], experiment, hBN defect						4.10	

B. C_BO_N

A carbon atom on a boron site and an oxygen atom on the adjacent nitrogen site form the C_BO_N defect, as depicted in Fig. 4(a). The inset in Fig. 4(a) shows that the N_2CO fragment in the urea molecule is the same as in the defect. Since urea is used to synthesize hBN flakes [45], this is additional motivation to study C_BO_N because it may originate from the growth process.

The defect breaks the planar symmetry: In the optimal ground-state geometry, the carbon atom and the oxygen atom bend out of plane, but in opposite directions (0.67 Å up and 0.77 Å down, respectively). Their distance from each other of 2.24 Å is drastically larger than the equilibrium distance of atoms on neighboring sites in hBN, which is 1.43 Å. We

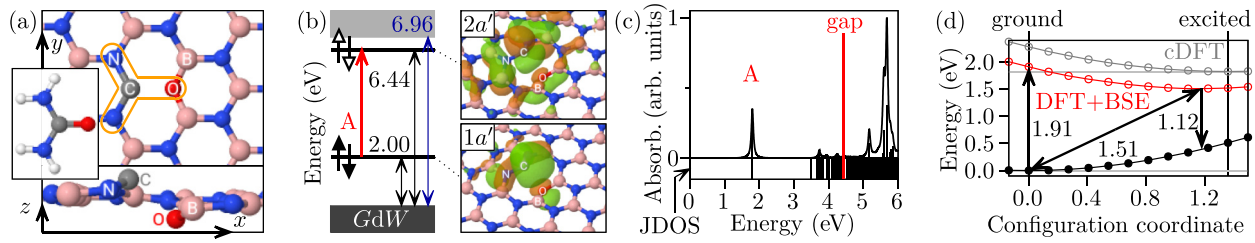

FIG. 4. Same as Fig. 3, but for C_BO_N. The system breaks planar symmetry. The inset in (a) shows the urea molecule. (b) The intragap defect states are labeled $1a'$ and $2a'$, and the transition "A" between them leads to a defect exciton at 1.91 eV. The spectrum in (c) is calculated with a cutoff energy of the plane wave basis of 3 Ry for Σ and K_d and 12 Ry for K_x. For the configuration coordinate diagram in (d) we extrapolated the exciton energy of the lowest defect exciton for an infinite cutoff energy for K_x. For numerical details, see the Supplemental Material [65].

note that the system is locally stable; i.e., forces vanish within numerical accuracy, and phonon frequencies are real. Furthermore, the observation of a Stark shift with an electric field that is not parallel to the layers of hBN [16] means that some defects may break the planar symmetry of the 2D material. The system maintains a mirror plain orthogonal to the y direction, but the symmetry breaking in the z direction leads to a reduction of the symmetry group to S_1 or C_S. To discuss the stability, we compare DFT total ground-state energies of the defect system and pristine hBN and chemical potentials of single atoms calculated from thermodynamically stable structures provided by the Open Quantum Materials Database [100,101]. According to these calculations, C_BO_N has a formation energy of 4.5 eV, which is below the formation energy of, e.g., V_N (8.3 eV) and C_N (5.0 eV). The heat of formation, however, does not include information about possible reaction paths, which would be required to discuss the probability that the urea molecule is incorporated in hBN during synthesis. We leave a detailed discussion to future work.

The ground state of C_BO_N is spin unpolarized. Inside the gap of hBN, the defect exhibits one occupied state and one empty state, 2.14 and 3.89 eV above the intrinsic valence band edge in LDA. In GdW, the energies are 2.00 and 6.44 eV, respectively [Fig. 4(b)]. Both states are symmetric towards reflection in the y direction, so we call them $1a'$ and $2a'$. The transition between them ("A") leads to a bright exciton at 1.91 eV [Fig. 4(c)]. While the lowest exciton of C_BC_N lies in the UV range (see Sec. IV A), C_BO_N emits at the energetically lower end of the visible spectrum. The reason for this is not only that the defect states of C_BO_N lie deeper inside the hBN gap but also that the electron-hole interaction is significantly larger compared to C_BC_N.

Relaxing the structure while keeping $1a'$ and $2a'$ occupied by one electron each, we obtain the excited state's optimal geometry, which does not differ qualitatively from the ground state's optimal geometry presented in Fig. 4(a): The carbon atom and the oxygen atom are still bent out of plane in opposite directions (0.53 Å up and 0.57 Å down, respectively). The total configuration coordinate ΔQ, however, is 1.36 amu$^{\frac{1}{2}}$ Å and thus more than 6 times larger than in the case of C_BC_N. The extent of the geometrical change between the ground and excited states is not only represented by ΔQ but also reflected by the difference between the electronic properties of the ground and excited states. The vertical transition energies $T_v = 1.91$ eV and $T_{v'} = 1.12$ eV [Fig. 4(d)], for example, differ much more compared to C_BC_N on relative and absolute scales. In contrast to C_BC_N, the DFT + BSE curve lies underneath the cDFT curve, and the minimum of the first is reached slightly earlier at 87% of the total configuration coordinate extent (instead of 90% in the case of C_BC_N). Nonetheless, BSE confirms the qualitative trend of the excited state's optimal geometry obtained from cDFT.

C. C_BV_N

Replacing one boron atom by a carbon atom and removing an adjacent nitrogen atom lead to the C_BV_N defect. A top view of this defect system is given in Fig. 5(a). Similar to C_BO_N, the planar symmetry is broken by the optimal ground state's geometry as the carbon atom bends out of plane, while a mirror plane orthogonal to the y direction is maintained and the symmetry group is S_1 (or C_S). The displacement of the carbon atom in the z direction is 0.61 Å. Noh *et al.* [16] and Gao *et al.* [33] showed with DFT-based calculations that nonplanar geometries are stable. Reimers *et al.* [30] performed a profound study on electronic configurations of C_BV_N with various methods, among them DFT and high-end wave function techniques. In their calculations, they found that the geometry which is lowest in energy is not planar (see the Supplemental Material of Ref. [30]). We note that C_BV_N is often analyzed in stable planar structures in the literature [27,28,102,103]. The reason for the ambiguity of the proposed equilibrium geometries is that this system has a much more complicated dependence of electronic structure on the geometry compared to the systems presented in the Secs. IV A and IV B, as we will see below.

As shown in Fig. 5(b), C_BV_N has one occupied and two empty intragap defect states. All of them are symmetric towards the mirror plane, so we label them $1a'$, $2a'$, and $3a'$. The electronic band gap between $1a'$ and $2a'$ strongly opens from 1.75 eV (LDA) to 4.23 eV (GdW). Both defect-defect transitions, which are possible between intragap defect states, lead to bright excitons at 1.79 and 3.06 eV (labeled A and B), as can be seen in the absorption spectrum in Fig. 5(c). These defect excitons are the lowest excitons of the system since the third-lowest exciton, which is dark, occurs at 3.50 eV. Our value for the distance of the occupied defect level to the intrinsic conduction band edge is in excellent agreement with Wang and Sundararaman [35]. Gao *et al.* found a slightly larger $1a'$-$2a'$ gap of 4.86 eV, which contributes to the fact that

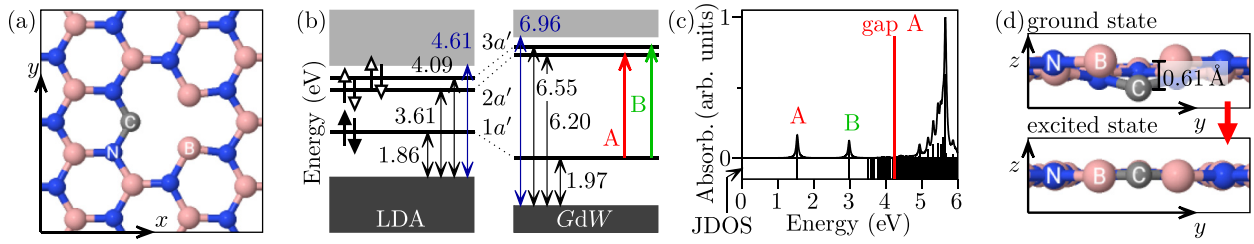

FIG. 5. C_BV_N. (a) Top view of the ground-state geometry. (b) Fully spin-degenerate single-particle energy levels in DFT-LDA and *GdW*, showing one occupied defect state and two empty intragap defect states, labeled $1a'$, $2a'$, and $3a'$. Arrows A and B indicate the transitions leading to defect excitons shown in (c) the absorption spectrum. Here, "gap A" refers to the single-particle energy distance between $1a'$ and $2a'$. To visualize dark states, we show the joint density of states (JDOS) underneath the absorption spectrum. The peak at 5.6 eV resembles the lowest exciton of intrinsic hBN (see Sec. IV A for discussion). (d) Side view of the defect: In the ground state, the carbon atom is bent out of plane. Relaxing the structure while keeping the electronic configuration in its excited state (cDFT), the carbon atom moves to the planar position.

their result of 2.61 eV for the lowest exciton is significantly larger.

Optimizing the geometry for the excited state ($1a'$ and $2a'$ populated by one electron each), we find striking differences from the ground-state structure: As can be seen in Fig. 5(d), the carbon atom moves to an in-plane position, in agreement with Ref. [16], although our optimal excited-state geometry is not exactly planar, with remaining vertical elongations of up to ∼0.2 Å. The total configuration coordinate is, with 3.47 amu$^{\frac{1}{2}}$ Å, roughly 2.5 times larger than ΔQ of C_BO_N and more than 16 times larger than ΔQ of C_BC_N. This drastic geometrical change affects the electronic properties, as depicted in Fig. 6(a). The real space representations of the three intragap defect states for the ground-state geometry in the left panels and the excited-state geometry in the right panels show qualitative differences. The central panel shows the evolution of the three defects states' energy levels if the geometry is linearly changed from the ground state's to the excited state's optimal geometry. The highest occupied level, $1a'$, and the lowest unoccupied level, $2a'$, become very close until the gap finally closes at the excited state's geometry and the system becomes metallic. However, we do not find significant differences between the wave functions for the ground state and the excited state at fixed geometry. Furthermore, in *GdW*/BSE, we observe no mixing of other DFT states with the relevant states $1a'$ and $2a'$. The changed electronic configuration limits our ability to practically perform the BSE calculations for two reasons. First, the distinction between valence and conduction states, which is necessary to set up the BSE Hamiltonian, becomes ambiguous. Second, the static screening approximation, which is used to calculate the direct part of the electron-hole interaction, is not proven to be valid for metallic systems. Furthermore, more complex excited-state configurations beyond the "singlet-excitation" concept of the BSE may occur in such situations (see, e.g., [104]), which is beyond the scope of this work. Therefore, the curve "DFT + BSE" in Fig. 6(b), which is obtained by adding the energy of the lowest exciton (transition A) to the ground-state total energy from DFT, stops at a certain point beyond which we consider the gap to be too small for a useful evaluation of the BSE. Reimers *et al.* [30] found for planar geometries that single-reference techniques (single Slater determinant) like DFT might be insufficient for C_BV_N. The metallic character of the excited-state geometry might thus be a result of the single-reference approach on which DFT is based, rather than its true electronic configuration.

Finally, we would like to discuss the relevance of C_BV_N for experiments on defect emission in hBN. The large number of theoretical studies on this defect is because C_BV_N has, compared to many other defects [64], spin-unpolarized, occupied, and empty intragap defect states and allows for bright transitions between them which lead to defect excitons in the visible regime. Some studies support the hypothesis that C_BV_N is responsible for the experimentally observed defect emission when comparing theoretical and experimental line shapes [27,28], but others do not [105,106]. We tend to

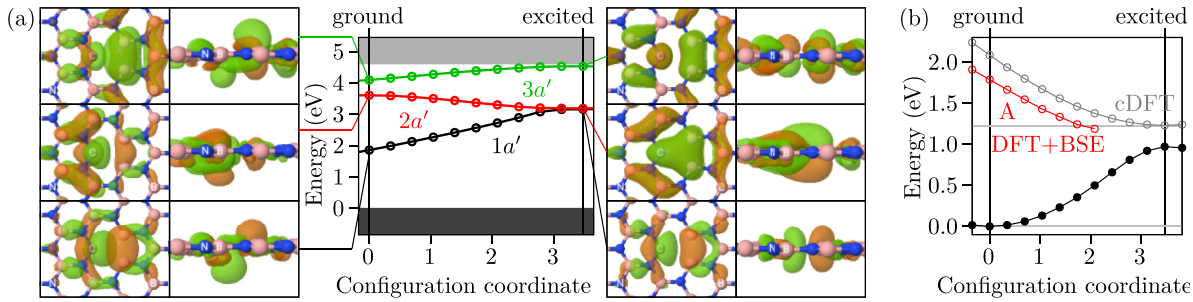

FIG. 6. C_BV_N. (a) The central panel shows the three defect states' energies as a function of the configuration coordinate [see caption of Fig. 3(d) for definition]. The six panels on the left show the top and side views of the defect states for the ground state's geometry, and the six panels on the right show the same for the excited state's geometry. (b) Configuration coordinate diagram similar to Fig. 3(d).

argue against the C_BV_N defect because the strong excited-state displacement (large ΔQ) and the strong dependence of the excitation energy on it would cause a large Stokes shift and possibly large peak broadening, both in the range of ∼1 eV. In contrast to the observations made in PLE experiments [23,24], the dominant peak in PLE would be noticeably blueshifted with respect to the ZPL.

V. BEYOND TAMM-DANCOFF APPROXIMATION

In the following, calculations going beyond the Tamm-Dancoff approximation, i.e., considering the coupling between resonant and antiresonant transitions, are referred to as the "full BSE." The resonant-antiresonant electron-hole interaction terms K^{AB} are usually dominated by the exchange part, which has an order of magnitude similar to the exchange part of the diagonal terms of K^{AA}. Hence, the following order is typical [82,107,108]:

$$\left|K_d^{AA}\right| > \left|K_x^{AA}\right| \sim \left|K_x^{AB}\right| > \left|K_d^{AB}\right|.$$

In spin-unpolarized systems, the exchange part enters only the singlet states. Thus, the TDA is usually a good approximation for the triplet states [109]. The enhancement of the singlet-state total energy by the exchange part goes along with a slightly larger spatial distance between the electron and hole. If the electron-hole wave function is spatially confined due to geometrical bounds, as, for instance, in molecules, the smaller distance between the electron and hole results in stronger interaction between them. The enhancement of electron-hole interaction due to spatial confinement affects the direct part as well as the exchange part. Hence, the TDA might give less reliable results for geometrically confined systems. We note in passing that for the CO molecule, we find the $^1\Pi$ exciton is 0.292 eV higher in the TDA compared to the value for T_v in Table I, which is similar to the findings of Çaylak and Baumeier [110].

As defect states are localized but embedded in an extended, crystalline solid, the question arises of how the TDA affects our calculated defect exciton energies. In Fig. 7(a), we compare the absorption spectrum of C_BO_N calculated within the TDA-BSE and the full BSE. Apparently, most excitons are hardly affected except for the lowest one, which is the strongly localized defect exciton and which is redshifted by approximately 0.55 eV in the full BSE compared to the TDA-BSE. Furthermore, we perform calculations beyond the TDA for C_BC_N, the carbon substitutions C_B and C_N, the nitrogen vacancy V_N, and the divacancy V_{NB} but not for C_BV_N, as this system requires more numerical effort. In Fig. 7(b), we plot the redshift in the full BSE $\Omega^{TDA} - \Omega^{full}$ over the expectation value of the exchange part of the electron-hole interaction $\langle K_x^{AA}\rangle$. The energies of the up to 100 energetically lowest excitons enter the data points presented in the graph. The data reveal that the difference between the TDA-BSE and full BSE indeed increases with growing exchange interaction, roughly given by $0.1\langle K_x^{AA}\rangle$ [see the dashed line in Fig. 7(b)]. As this estimate is valid for six different systems, we assume that it should also apply to the numerically more demanding C_BV_N, whose lowest defect exciton has $\langle K_x^{AA}\rangle = 1$ eV, similar to C_BO_N. We note that this trend would be less clear if we plotted $\Omega^{TDA} - \Omega^{full}$ over the direct part of the electron-hole interaction. For defect systems other than C_BO_N, the difference between the TDA-BSE and full BSE is smaller, and the largest difference is observed for the lowest defect exciton: 0.11 eV for C_BC_N, 0.08 eV for V_{NB}, 0.06 eV for V_N, 0.03 eV for C_N, and 0.02 eV for C_B. Although the differences from the full BSE of the systems presented in this work do not seem to be negligible, they do not impose qualitative changes to the configuration coordinate diagrams in the previous sections. For C_B, C_N, V_N, and V_{NB}, the differences between the full and TDA-BSE are smaller compared to those of the other defects because they do not allow for bright transitions between intragap defect states and the bulk bands of intrinsic hBN are always involved.

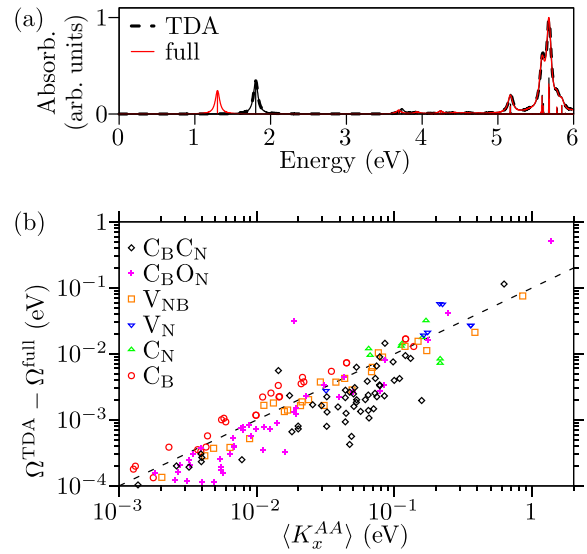

FIG. 7. (a) Absorption spectrum of C_BO_N with and without TDA as an example. (b) Differences between TDA- and full-BSE calculations plotted over the exchange part of the electron-hole interaction $\langle K_x^{AA}\rangle$. The data points are from the lowest up to 100 excitons of different hBN defects. The dashed line is a guide to the eye for $0.1\langle K_x^{AA}\rangle$.

VI. CONCLUSION

As a starting point, we calculated excited-state curves of carbon monoxide within GW + BSE. Our results were in reasonable agreement with previous calculations. In the main part, we used (c)DFT to optimize the structure for the electronic ground state and the first excited state of three defects in hBN: C_BC_N, C_BO_N, and C_BV_N. For the ground and excited states' optimal geometry as well as for a few intermediate geometries between them, we performed GdW + BSE calculations and used the exciton energy of a transition assigned to the excited state to obtain a more reliable value for the excited-state total energy. All systems investigated in this paper possess interesting properties as they allow for bright transitions between intragap defect states. For C_BC_N and C_BO_N, we found good agreement between cDFT and BSE regarding the minimum of the excited-state curve as a function of the configuration coordinate. C_BC_N has shallow defect states, emits UV light, is planar, and depends weakly on geometry. In contrast, C_BO_N and C_BV_N have deep defect states, emit in the low visible regime, break planar symmetry, and

show strong geometrical dependence. Apparently, the nonplanarity allows for more structural changes after excitation and therefore leads to a stronger dependence of electronic properties on geometry. It is this strong geometrical dependence which makes C_BO_N and C_BV_N unlikely to be responsible for the hBN defect emission observed in experiments where the Stokes shift is small. In the final section, we showed that TDA might lead to non-negligible quantitative changes in calculated excitons for localized defects, which, however, did not result in qualitative changes.

ACKNOWLEDGMENTS

T.D. acknowledges financial support from the Deutsche Forschungsgemeinschaft (DFG, German Research Foundation) through Project No. 426726249 (DE 2749/2-1 and DE 2749/2-2). The authors gratefully acknowledge the Gauss Centre for Supercomputing e.V. [111] for funding this project by providing computing time through the John von Neumann Institute for Computing on the GCS Supercomputer JUWELS [112] at Jülich Supercomputing Centre.

[1] Y. Kubota, K. Watanabe, O. Tsuda, and T. Taniguchi, Deep ultraviolet light-emitting hexagonal boron nitride synthesized at atmospheric pressure, Science **317**, 932 (2007).

[2] T. T. Tran, K. Bray, M. J. Ford, M. Toth, and I. Aharonovich, Quantum emission from hexagonal boron nitride monolayers, Nat. Nanotechnol. **11**, 37 (2016).

[3] A. Kubanek, Coherent quantum emitters in hexagonal boron nitride, Adv. Quantum Technol. **5**, 2200009 (2022).

[4] M. E. Turiansky, A. Alkauskas, and C. G. Van de Walle, Spinning up quantum defects in 2D materials, Nat. Mater. **19**, 487 (2020).

[5] S. Choi, T. T. Tran, C. Elbadawi, C. Lobo, X. Wang, S. Juodkazis, G. Seniutinas, M. Toth, and I. Aharonovich, Engineering and localization of quantum emitters in large hexagonal boron nitride layers, ACS Appl. Mater. Interfaces **8**, 29642 (2016).

[6] N. Chejanovsky, M. Rezai, F. Paolucci, Y. Kim, T. Rendler, W. Rouabeh, F. Fávaro de Oliveira, P. Herlinger, A. Denisenko, S. Yang, I. Gerhardt, A. Finkler, J. H. Smet, and J. Wrachtrup, Structural attributes and photodynamics of visible spectrum quantum emitters in hexagonal boron nitride, Nano Lett. **16**, 7037 (2016).

[7] Y. Chen, X. Xu, C. Li, A. Bendavid, M. T. Westerhausen, C. Bradac, M. Toth, I. Aharonovich, and T. T. Tran, Bottom-up synthesis of hexagonal boron nitride nanoparticles with intensity-stabilized quantum emitters, Small **17**, 2008062 (2021).

[8] C. Zhang, Z. Shi, T. Wu, and X. Xie, Microstructure engineering of hexagonal boron nitride for single-photon emitter applications, Adv. Opt. Mater. **10**, 2200207 (2022).

[9] A. Gale, C. Li, Y. Chen, K. Watanabe, T. Taniguchi, I. Aharonovich, and M. Toth, Site-specific fabrication of blue quantum emitters in hexagonal boron nitride, ACS Photonics **9**, 2170 (2022).

[10] A. Kumar, C. Cholsuk, A. Zand, M. N. Mishuk, T. Matthes, F. Eilenberger, S. Suwanna, and T. Vogl, Localized creation of yellow single photon emitting carbon complexes in hexagonal boron nitride, APL Mater. **11**, 071108 (2023).

[11] A. B. D. Shaik and P. Palla, Optical quantum technologies with hexagonal boron nitride single photon sources, Sci. Rep. **11**, 12285 (2021).

[12] H. Akbari, S. Biswas, P. K. Jha, J. Wong, B. Vest, and H. A. Atwater, Lifetime-limited and tunable quantum light emission in h-BN via electric field modulation, Nano Lett. **22**, 7798 (2022).

[13] G. Grosso, H. Moon, B. Lienhard, S. Ali, D. K. Efetov, M. M. Furchi, P. Jarillo-Herrero, M. J. Ford, I. Aharonovich, and D. Englund, Tunable and high-purity room temperature single-photon emission from atomic defects in hexagonal boron nitride, Nat. Commun. **8**, 705 (2017).

[14] N. Mendelson, M. Doherty, M. Toth, I. Aharonovich, and T. T. Tran, Strain-induced modification of the optical characteristics of quantum emitters in hexagonal boron nitride, Adv. Mater. **32**, 1908316 (2020).

[15] F. Wu, T. J. Smart, J. Xu, and Y. Ping, Carrier recombination mechanism at defects in wide band gap two-dimensional materials from first principles, Phys. Rev. B **100**, 081407(R) (2019).

[16] G. Noh, D. Choi, J.-H. Kim, D.-G. Im, Y.-H. Kim, H. Seo, and J. Lee, Stark tuning of single-photon emitters in hexagonal boron nitride, Nano Lett. **18**, 4710 (2018).

[17] C. Jara, T. Rauch, S. Botti, M. A. L. Marques, A. Norambuena, R. Coto, J. E. Castellanos-Águila, J. R. Maze, and F. Munoz, First-principles identification of single photon emitters based on carbon clusters in hexagonal boron nitride, J. Phys. Chem. A **125**, 1325 (2021).

[18] A. Sajid, K. S. Thygesen, J. R. Reimers, and M. J. Ford, Edge effects on optically detected magnetic resonance of vacancy defects in hexagonal boron nitride, Commun. Phys. **3**, 153 (2020).

[19] A. Alkauskas, J. L. Lyons, D. Steiauf, and C. G. Van de Walle, First-principles calculations of luminescence spectrum line shapes for defects in semiconductors: The example of GaN and ZnO, Phys. Rev. Lett. **109**, 267401 (2012).

[20] D. Wigger, R. Schmidt, O. D. Pozo-Zamudio, J. A. Preuß, P. Tonndorf, R. Schneider, P. Steeger, J. Kern, Y. Khodaei, J. Sperling, S. M. de Vasconcellos, R. Bratschitsch, and T. Kuhn, Phonon-assisted emission and absorption of individual color centers in hexagonal boron nitride, 2D Mater. **6**, 035006 (2019).

[21] D. K. Lewis, A. Ramasubramaniam, and S. Sharifzadeh, Tuned and screened range-separated hybrid density functional theory for describing electronic and optical properties of defective gallium nitride, Phys. Rev. Mater. **4**, 063803 (2020).

[22] I. Niehues, P. Marauhn, T. Deilmann, D. Wigger, R. Schmidt, A. Arora, S. Michaelis de Vasconcellos, M. Rohlfing, and R. Bratschitsch, Strain tuning of the Stokes shift in atomically thin semiconductors, Nanoscale **12**, 20786 (2020).

[23] G. Grosso, H. Moon, C. J. Ciccarino, J. Flick, N. Mendelson, L. Mennel, M. Toth, I. Aharonovich, P. Narang, and D. R. Englund, Low-temperature electron–phonon interaction of

quantum emitters in hexagonal boron nitride, ACS Photonics **7**, 1410 (2020).

[24] R. N. E. Malein, P. Khatri, A. J. Ramsay, and I. J. Luxmoore, Stimulated emission depletion spectroscopy of color centers in hexagonal boron nitride, ACS Photonics **8**, 1007 (2021).

[25] M. E. Turiansky, A. Alkauskas, L. C. Bassett, and C. G. Van de Walle, Dangling bonds in hexagonal boron nitride as single-photon emitters, Phys. Rev. Lett. **123**, 127401 (2019).

[26] M. Mackoit-Sinkevičienė, M. Maciaszek, C. G. Van de Walle, and A. Alkauskas, Carbon dimer defect as a source of the 4.1 eV luminescence in hexagonal boron nitride, Appl. Phys. Lett. **115**, 212101 (2019).

[27] A. Sajid and K. S. Thygesen, VNCB defect as source of single photon emission from hexagonal boron nitride, 2D Mater. **7**, 031007 (2020).

[28] S. A. Tawfik, S. Ali, M. Fronzi, M. Kianinia, T. T. Tran, C. Stampfl, I. Aharonovich, M. Toth, and M. J. Ford, First-principles investigation of quantum emission from hBN defects, Nanoscale **9**, 13575 (2017).

[29] J. Gavnholt, T. Olsen, M. Engelund, and J. Schiøtz, Δ self-consistent field method to obtain potential energy surfaces of excited molecules on surfaces, Phys. Rev. B **78**, 075441 (2008).

[30] J. R. Reimers, A. Sajid, R. Kobayashi, and M. J. Ford, Understanding and calibrating density-functional-theory calculations describing the energy and spectroscopy of defect sites in hexagonal boron nitride, J. Chem. Theory Comput. **14**, 1602 (2018).

[31] A. Sajid, M. J. Ford, and J. R. Reimers, Single-photon emitters in hexagonal boron nitride: A review of progress, Rep. Prog. Phys. **83**, 044501 (2020).

[32] C. Attaccalite, M. Bockstedte, A. Marini, A. Rubio, and L. Wirtz, Coupling of excitons and defect states in boron-nitride nanostructures, Phys. Rev. B **83**, 144115 (2011).

[33] S. Gao, H.-Y. Chen, and M. Bernardi, Radiative properties of quantum emitters in boron nitride from excited state calculations and Bayesian analysis, npj Comput. Mater. **7**, 85 (2021).

[34] N. Berseneva, A. Gulans, A. V. Krasheninnikov, and R. M. Nieminen, Electronic structure of boron nitride sheets doped with carbon from first-principles calculations, Phys. Rev. B **87**, 035404 (2013).

[35] D. Wang and R. Sundararaman, Layer dependence of defect charge transition levels in two-dimensional materials, Phys. Rev. B **101**, 054103 (2020).

[36] F. Wu, A. Galatas, R. Sundararaman, D. Rocca, and Y. Ping, First-principles engineering of charged defects for two-dimensional quantum technologies, Phys. Rev. Mater. **1**, 071001(R) (2017).

[37] Y. Chen and S. Y. Quek, Photophysical characteristics of boron vacancy-derived defect centers in hexagonal boron nitride, J. Phys. Chem. C **125**, 21791 (2021).

[38] Y. Ma and M. Rohlfing, Optical excitation of deep defect levels in insulators within many-body perturbation theory: The F center in calcium fluoride, Phys. Rev. B **77**, 115118 (2008).

[39] N. Mendelson, D. Chugh, J. R. Reimers, T. S. Cheng, A. Gottscholl, H. Long, C. J. Mellor, A. Zettl, V. Dyakonov, P. H. Beton, S. V. Novikov, C. Jagadish, H. H. Tan, M. J. Ford, M. Toth, C. Bradac, and I. Aharonovich, Identifying carbon as the source of visible single-photon emission from hexagonal boron nitride, Nat. Mater. **20**, 321 (2021).

[40] M. Fischer, J. M. Caridad, A. Sajid, S. Ghaderzadeh, M. Ghorbani-Asl, L. Gammelgaard, P. Bøggild, K. S. Thygesen, A. V. Krasheninnikov, S. Xiao, M. Wubs, and N. Stenger, Controlled generation of luminescent centers in hexagonal boron nitride by irradiation engineering, Sci. Adv. **7**, eabe7138 (2021).

[41] S. Zhang, K. Li, C. Guo, and Y. Ping, Effect of environmental screening and strain on optoelectronic properties of two-dimensional quantum defects, 2D Mater. **10**, 035036 (2023).

[42] T. Taniguchi and K. Watanabe, Synthesis of high-purity boron nitride single crystals under high pressure by using Ba–BN solvent, J. Cryst. Growth **303**, 525 (2007).

[43] R. Sevak Singh, R. Yingjie Tay, W. Leong Chow, S. Hon Tsang, G. Mallick, and E. H. Tong Teo, Band gap effects of hexagonal boron nitride using oxygen plasma, Appl. Phys. Lett. **104**, 163101 (2014).

[44] N. L. McDougall, J. G. Partridge, R. J. Nicholls, S. P. Russo, and D. G. McCulloch, Influence of point defects on the near edge structure of hexagonal boron nitride, Phys. Rev. B **96**, 144106 (2017).

[45] B. Matović, J. Luković, M. Nikolić, B. Babić, N. Stanković, B. Jokić, and B. Jelenković, Synthesis and characterization of nanocrystaline hexagonal boron nitride powders: XRD and luminescence properties, Ceram. Int. **42**, 16655 (2016).

[46] I. N. Yakovkin and P. A. Dowben, The problem of the band gap in LDA calculations, Surf. Rev. Lett. **14**, 481 (2007).

[47] D. M. Ceperley and B. J. Alder, Ground state of the electron gas by a stochastic method, Phys. Rev. Lett. **45**, 566 (1980).

[48] L. M. Sandratskii, Noncollinear magnetism in itinerant-electron systems: Theory and applications, Adv. Phys. **47**, 91 (1998).

[49] L. Kleinman and D. M. Bylander, Efficacious form for model pseudopotentials, Phys. Rev. Lett. **48**, 1425 (1982).

[50] G. B. Bachelet, D. R. Hamann, and M. Schlüter, Pseudopotentials that work: From H to Pu, Phys. Rev. B **26**, 4199 (1982).

[51] D. R. Hamann, Generalized norm-conserving pseudopotentials, Phys. Rev. B **40**, 2980 (1989).

[52] D. R. Hamann, M. Schlüter, and C. Chiang, Norm-conserving pseudopotentials, Phys. Rev. Lett. **43**, 1494 (1979).

[53] J. Wieferink, P. Krüger, and J. Pollmann, Improved hybrid algorithm with Gaussian basis sets and plane waves: First-principles calculations of ethylene adsorption on β-SiC(001)-(3 $\times$ 2), Phys. Rev. B **74**, 205311 (2006).

[54] W. Kohn and L. J. Sham, Self-consistent equations including exchange and correlation effects, Phys. Rev. **140**, A1133 (1965).

[55] J. P. Perdew and A. Zunger, Self-interaction correction to density-functional approximations for many-electron systems, Phys. Rev. B **23**, 5048 (1981).

[56] R. O. Jones and O. Gunnarsson, The density functional formalism, its applications and prospects, Rev. Mod. Phys. **61**, 689 (1989).

[57] A. Hellman, B. Razaznejad, and B. I. Lundqvist, Potential-energy surfaces for excited states in extended systems, J. Chem. Phys. **120**, 4593 (2004).

[58] J. Mu, Y. Ma, H. Yin, C. Liu, and M. Rohlfing, Photoluminescence of single-walled carbon nanotubes: The role of stokes shift and impurity levels, Phys. Rev. Lett. **111**, 137401 (2013).

[59] M. Bockstedte, F. Schütz, T. Garratt, V. Ivády, and A. Gali, Ab initio description of highly correlated states in de-

fects for realizing quantum bits, npj Quantum Mater. **3**, 31 (2018).
[60] P. Krüger and J. Pollmann, Self-consistent surface electronic structure for semi-infinite semiconductors from scattering theory, Phys. B (Amsterdam, Neth.) **172**, 155 (1991).
[61] Y. Jia, S. Poncé, A. Miglio, M. Mikami, and X. Gonze, Beyond the one-dimensional configuration coordinate model of photoluminescence, Phys. Rev. B **100**, 155109 (2019).
[62] L. Hedin, New method for calculating the one-particle Green's function with application to the electron-gas problem, Phys. Rev. **139**, A796 (1965).
[63] M. S. Hybertsen and S. G. Louie, Electron correlation in semiconductors and insulators: Band gaps and quasiparticle energies, Phys. Rev. B **34**, 5390 (1986).
[64] A. Kirchhoff, T. Deilmann, P. Krüger, and M. Rohlfing, Electronic and optical properties of a hexagonal boron nitride monolayer in its pristine form and with point defects from first principles, Phys. Rev. B **106**, 045118 (2022).
[65] See Supplemental Material at http://link.aps.org/supplemental/10.1103/PhysRevB.109.085127 for details on methods and numerics, real space representations of intragap defect states, and atom positions of defect cells, which also includes Refs. [53,60,64,66,67,84,100,101,113–117].
[66] M. Rohlfing, P. Krüger, and J. Pollmann, Efficient scheme for *GW* quasiparticle band-structure calculations with applications to bulk Si and to the Si(001)-(2 × 1) surface, Phys. Rev. B **52**, 1905 (1995).
[67] M. Rohlfing, P. Krüger, and J. Pollmann, Quasiparticle band-structure calculations for C, Si, Ge, GaAs, and SiC using Gaussian-orbital basis sets, Phys. Rev. B **48**, 17791 (1993).
[68] M. Rohlfing, Electronic excitations from a perturbative LDA + *GdW* approach, Phys. Rev. B **82**, 205127 (2010).
[69] C. S. Wang and W. E. Pickett, Density-functional theory of excitation spectra of semiconductors: Application to Si, Phys. Rev. Lett. **51**, 597 (1983).
[70] F. Gygi and A. Baldereschi, Quasiparticle energies in semiconductors: Self-energy correction to the local-density approximation, Phys. Rev. Lett. **62**, 2160 (1989).
[71] V. Fiorentini and A. Baldereschi, Dielectric scaling of the self-energy scissor operator in semiconductors and insulators, Phys. Rev. B **51**, 17196 (1995).
[72] M. Drüppel, T. Deilmann, J. Noky, P. Marauhn, P. Krüger, and M. Rohlfing, Electronic excitations in transition metal dichalcogenide monolayers from an LDA + *GdW* approach, Phys. Rev. B **98**, 155433 (2018).
[73] F. Bechstedt, R. Enderleln, and R. Wischnewski, Binding energies and chemical shifts of least bound core electron excitations in cubic A_NB_{8-N} semiconductors, Phys. Status Solidi B **107**, 637 (1981).
[74] D. L. Johnson, Local field effects and the dielectric response matrix of insulators: A model, Phys. Rev. B **9**, 4475 (1974).
[75] P. Larson, M. Dvorak, and Z. Wu, Role of the plasmon-pole model in the *GW* approximation, Phys. Rev. B **88**, 125205 (2013).
[76] T. Deilmann, Valley selectivity induced by magnetic adsorbates: Triplet oxygen on monolayer MoS_2, Phys. Rev. B **101**, 085130 (2020).
[77] T. Deilmann and K. S. Thygesen, Unraveling the not-so-large trion binding energy in monolayer black phosphorus, 2D Mater. **5**, 041007 (2018).
[78] G. Strinati, Dynamical shift and broadening of core excitons in semiconductors, Phys. Rev. Lett. **49**, 1519 (1982).
[79] G. Strinati, Effects of dynamical screening on resonances at inner-shell thresholds in semiconductors, Phys. Rev. B **29**, 5718 (1984).
[80] G. Onida, L. Reining, and A. Rubio, Electronic excitations: density-functional versus many-body Green's-function approaches, Rev. Mod. Phys. **74**, 601 (2002).
[81] M. Rohlfing and S. G. Louie, Electron-hole excitations and optical spectra from first principles, Phys. Rev. B **62**, 4927 (2000).
[82] T. Lettmann and M. Rohlfing, Electronic excitations of polythiophene within many-body perturbation theory with and without the Tamm–Dancoff approximation, J. Chem. Theory Comput. **15**, 4547 (2019).
[83] S. Hirata and M. Head-Gordon, Time-dependent density functional theory within the Tamm–Dancoff approximation, Chem. Phys. Lett. **314**, 291 (1999).
[84] T. Förster, P. Krüger, and M. Rohlfing, Two-dimensional topological phases and electronic spectrum of Bi_2Se_3 thin films from *GW* calculations, Phys. Rev. B **92**, 201404(R) (2015).
[85] D. J. Tozer and N. C. Handy, Improving virtual Kohn–Sham orbitals and eigenvalues: Application to excitation energies and static polarizabilities, J. Chem. Phys. **109**, 10180 (1998).
[86] S. G. Lias, Ionization energy evaluation, in *NIST Chemistry WebBook*, edited by P. Linstrom and W. Mallard, NIST Standard Reference Database No. 69 (National Institute of Standards and Technology, Gaithersburg, MD, 2023).
[87] S. Ismail-Beigi and S. G. Louie, Excited-state forces within a first-principles Green's function formalism, Phys. Rev. Lett. **90**, 076401 (2003).
[88] J. A. Hall, J. Schamps, J. M. Robbe, and H. Lefebvre-Brion, Theoretical study of the perturbation parameters in the a $^3\Pi$ and A $^1\Pi$ states of CO, J. Chem. Phys. **59**, 3271 (1973).
[89] K. P. Huber and G. H. Herzberg, Constants of diatomic molecules, in *NIST Chemistry WebBook*, edited by P. Linstrom and W. Mallard, NIST Standard Reference Database No. 69 (National Institute of Standards and Technology, Gaithersburg, MD, 2023). Data prepared by Jean W. Gallagher and Russell D. Johnson III.
[90] J. F. Stanton, J. Gauss, N. Ishikawa, and M. Head-Gordon, A comparison of single reference methods for characterizing stationary points of excited state potential energy surfaces, J. Chem. Phys. **103**, 4160 (1995).
[91] F. Wang and F. P. Larkins, Influence of ground-state geometry on carbon monoxide x-ray emission spectral profiles, J. Phys. B **31**, 3513 (1998).
[92] A. Bosak, J. Serrano, M. Krisch, K. Watanabe, T. Taniguchi, and H. Kanda, Elasticity of hexagonal boron nitride: Inelastic x-ray scattering measurements, Phys. Rev. B **73**, 041402(R) (2006).
[93] K. Ba, W. Jiang, J. Cheng, J. Bao, N. Xuan, Y. Sun, B. Liu, A. Xie, S. Wu, and Z. Sun, Chemical and bandgap engineering in monolayer hexagonal boron nitride, Sci. Rep. **7**, 45584 (2017).
[94] C. Elias, P. Valvin, T. Pelini, A. Summerfield, C. J. Mellor, T. S. Cheng, L. Eaves, C. T. Foxon, P. H. Beton, S. V. Novikov,

B. Gil, and G. Cassabois, Direct band-gap crossover in epitaxial monolayer boron nitride, Nat. Commun. **10**, 2639 (2019).

[95] Y. Stehle III, H. M. Meyer, R. R. Unocic, M. Kidder, G. Polizos, P. G. Datskos, R. Jackson, S. N. Smirnov, and I. V. Vlassiouk, Synthesis of hexagonal boron nitride monolayer: Control of nucleation and crystal morphology, Chem. Mater. **27**, 8041 (2015).

[96] L. Museur, E. Feldbach, and A. Kanaev, Defect-related photoluminescence of hexagonal boron nitride, Phys. Rev. B **78**, 155204 (2008).

[97] R. Bourrellier, S. Meuret, A. Tararan, O. Stéphan, M. Kociak, L. H. G. Tizei, and A. Zobelli, Bright UV single photon emission at point defects in *h*-BN, Nano Lett. **16**, 4317 (2016).

[98] C. Linderälv, W. Wieczorek, and P. Erhart, Vibrational signatures for the identification of single-photon emitters in hexagonal boron nitride, Phys. Rev. B **103**, 115421 (2021).

[99] M. Winter, M. H. E. Bousquet, D. Jacquemin, I. Duchemin, and X. Blase, Photoluminescent properties of the carbon-dimer defect in hexagonal boron-nitride: A many-body finite-size cluster approach, Phys. Rev. Mater. **5**, 095201 (2021).

[100] J. E. Saal, S. Kirklin, M. Aykol, B. Meredig, and C. Wolverton, Materials design and discovery with high-throughput density functional theory: The Open Quantum Materials Database (OQMD), JOM **65**, 1501 (2013).

[101] S. Kirklin, J. E. Saal, B. Meredig, A. Thompson, J. W. Doak, M. Aykol, S. Rühl, and C. Wolverton, The Open Quantum Materials Database (OQMD): Assessing the accuracy of DFT formation energies, npj Comput. Mater. **1**, 15010 (2015).

[102] A. Sajid, J. R. Reimers, and M. J. Ford, Defect states in hexagonal boron nitride: Assignments of observed properties and prediction of properties relevant to quantum computation, Phys. Rev. B **97**, 064101 (2018).

[103] D. S. Wang, C. J. Ciccarino, J. Flick, and P. Narang, Hybridized defects in solid-state materials as artificial molecules, ACS Nano **15**, 5240 (2021).

[104] S. K. Choi, M. Jain, and S. G. Louie, Mechanism for optical initialization of spin in NV^- center in diamond, Phys. Rev. B **86**, 041202(R) (2012).

[105] M. Fischer, A. Sajid, J. Iles-Smith, A. Hötger, D. I. Miakota, M. K. Svendsen, C. Kastl, S. Canulescu, S. Xiao, M. Wubs, K. S. Thygesen, A. W. Holleitner, and N. Stenger, Combining experiments on luminescent centres in hexagonal boron nitride with the polaron model and ab initio methods towards the identification of their microscopic origin, Nanoscale **15**, 14215 (2023).

[106] S. Li and A. Gali, Bistable carbon-vacancy defects in *h*-BN, Frontiers Quantum Sci. Technol. **1**, 1007756 (2022).

[107] K. Ohno, Optical properties of alkali-earth atoms and Na_2 calculated by GW and Bethe–Salpeter equations, Science Technol. Adv. Mater. **5**, 603 (2004).

[108] Y. Ma, M. Rohlfing, and C. Molteni, Excited states of biological chromophores studied using many-body perturbation theory: Effects of resonant-antiresonant coupling and dynamical screening, Phys. Rev. B **80**, 241405(R) (2009).

[109] T. Lettmann and M. Rohlfing, Finite-momentum excitons in rubrene single crystals, Phys. Rev. B **104**, 115427 (2021).

[110] O. Çaylak and B. Baumeier, Excited-state geometry optimization of small molecules with many-body Green's functions theory, J. Chem. Theory Comput. **17**, 879 (2021).

[111] www.gauss-centre.eu.

[112] D. Alvarez, JUWELS Cluster and Booster: Exascale pathfinder with modular supercomputing architecture at Juelich Supercomputing Centre, J. Large-Scale Res. Facil. **7**, A183 (2021).

[113] M.-C. Heißenbüttel, T. Deilmann, P. Krüger, and M. Rohlfing, Valley-dependent interlayer excitons in magnetic WSe_2/CrI_3, Nano Lett. **21**, 5173 (2021).

[114] P. M. Morse, Diatomic molecules according to the wave mechanics. II. Vibrational levels, Phys. Rev. **34**, 57 (1929).

[115] C. L. Pekeris, The rotation-vibration coupling in diatomic molecules, Phys. Rev. **45**, 98 (1934).

[116] H. J. Monkhorst and J. D. Pack, Special points for Brillouin-zone integrations, Phys. Rev. B **13**, 5188 (1976).

[117] L. Wirtz, A. Marini, and A. Rubio, Excitons in boron nitride nanotubes: Dimensionality effects, Phys. Rev. Lett. **96**, 126104 (2006).